



Investigation of static wings interacting with vertical gusts of indefinite length at low Reynolds numbers

Colin Stutz¹ · John Hrynuk² · Douglas Bohl¹

Received: 9 February 2022 / Revised: 30 March 2022 / Accepted: 1 April 2022 / Published online: 12 May 2022
© The Author(s), under exclusive licence to Springer-Verlag GmbH Germany, part of Springer Nature 2022

Abstract

A novel gust generator was developed to study the interaction of wings with vertical gusts of controllable interaction time with magnitudes up to 30% of the freestream velocity at low Reynolds numbers. This work focuses on the collection of force and flow field data for three airfoils entering vertical gusts. Full-span NACA 0012, Eppler 387, and SD 5060 airfoils were tested with gusts of 20 and 30% of the freestream velocity at a Reynolds number of 12×10^3 and 20% of the freestream at a Reynolds number of 54.4×10^3 . The lift generated during the gust interactions showed rapid increases in lift, often with a short-lived overshoot above the steady-state lift at the lower Reynolds number. Accompanying flow field data showed that the overshoot in lift was caused by a reattachment of the flow at the trailing edge of the symmetric NACA 0012, which was observed as a deflection of the streamlines in the freestream flow direction for the cambered airfoils. A new model was created to predict the lift during the interaction, which uses the static lift curve to predict the lift at a given effective flow angle, with corrections to account for the rate of change of the flow angle and camber of the airfoil. This model was able to more accurately predict the lift during gust interactions than the currently used modified Goman–Khrabrov model, while remaining a simple model to implement.

1 Introduction

Advances in technology have enabled the development and proliferation of small-scale Unmanned Aircraft Systems (UAS). These small UAS (sUAS) inhabit much more hostile flow regimes compared to their manned counterparts. Vertical gusts, sometimes on the scale of the vehicle's forward velocity, have become an operational concern for these aircraft in part because sUAS tend to fly at much lower altitudes than regular aircraft where large-scale turbulence and windy conditions are more prevalent (Mueller and DeLaurier 2001;

Jing et al. 2020; Flay et al. 1982; Bohrer et al. 2012). The ability to maneuver within a gusty urban environment, and others like it, is key to operating sUAS in the future. Modern vehicle control algorithms respond to gusts as a disturbance in need of correction (Hamada et al. 2019), whereas many flying and swimming animals are known to passively react to, maneuver through, or even take advantage of dynamic flow conditions (Bohrer et al. 2012; Fish and Lauder 2006; Lentink et al. 2007; Newman 1958; Quinn et al. 2019; Tucker 1987). The aerodynamic impact of these unsteady conditions on vehicle flight needs to be understood before a vehicle controller can be programmed to take advantage of them instead of expending energy to counter them.

Localized updrafts and downdrafts in the atmospheric boundary layer have been measured on the order of a typical sUAS's forward flight speed (Kussner 1935) and these gusts can lead to highly transient changes in flow angle, $\alpha_{f_{low}}$, of 5 to 15 degrees (Watkins et al. 2006). For comparison, full-scale aircraft typically experience gust velocities below 5% of their forward speed (Skinn et al. 1996; Rutensburg et al. 2002), or $\alpha_{f_{low}}$ less than 3 degrees. Gusts are typically characterized by this updraft velocity to forward speed ratio, more commonly referred to as the gust ratio (GR), where $GR = v/u$ and u and v are velocity components in the

✉ Colin Stutz
stutzcm@clarkson.edu

John Hrynuk
john.t.hrynuk.civ@army.mil

Douglas Bohl
dbohl@clarkson.edu

¹ Department of Mechanical and Aerospace Engineering, Clarkson University, 8 Clarkson Ave. Box 5725, Potsdam, NY 13699, USA

² Weapons and Materials Research Directorate, US Army Research Lab, 6340 Rodman Rd, Aberdeen Proving Ground, MD 21005, USA

x and y directions, respectively. Larger gust ratios are present in more unsteady environments or at lower flight speeds. Environmental conditions that generate the strongest natural gusts are found in urban environments where updrafts are created around buildings and “street canyons” can create high winds and downdrafts (Watkins et al. 2006; Golubev and Visbal 2012; White et al. 2012; Dabberdt et al. 1973). A computational analysis by Watkins et al. (2019) found that these updrafts around buildings can lead to flow angles of up to 45 degrees.

The most common forms of gust generation in lab settings are oscillating vanes in water or wind tunnels (Garby et al. 1957; Buell 1969; Lancelot et al. 2015; Young and Smith 2020) and stationary jets in a tow-tank (Corkery et al. 2018a, b; Biler and Jones 2020; Perotta and Jones 2017). Common oscillating vane generators use a single airfoil or a vertical array of airfoils oscillating in unison, which sends large vortices downstream toward the model. This creates a sinusoidal gust profile, which is ideal for creating aerodynamic loading cycles. However, the interaction between the model and any one vertical disturbance is short. Stationary jets in tow tanks allow for investigating single wing-gust interactions but are limited in the physical size of the jet and therefore the length of the wing-gust interaction at any given Reynolds number. The width of the gust jet is often on the order of the model chord, limiting these generators to the study of highly transient gusts.

This study details the use of a novel gust generator, the Actuated Recirculating Gust Generator for sUAS Studies (ARGGUS), to evaluate the force history of gusts that closely mimic real-world conditions. The ARGGUS uses a vertical jet in a wind tunnel that can be actuated on or off, allowing for gusts of arbitrary interaction time. This gust generator was used to collect force data on three airfoils (NACA 0012, Eppler 387, and SD 5060) as they encountered gusts. Flow field data was also collected via particle image velocimetry (PIV) to study the gust-wing interactions. Finally, this work documents the development of a new force prediction model for wing-gust interactions that was able to better predict the measured forces than the commonly used adaptation of the Goman–Khrabrov (G-K) model.

2 Experimental methods

2.1 Actuated recirculating gust generator for sUAS studies (ARGGUS)

The ARGGUS was designed to integrate with the Army Research Lab’s (ARL) Microsystem Aeromechanics Wind Tunnel (MAWT), with the gust outlet located in the floor of the test section, see Fig. 1. The gust is generated by a high velocity jet in cross flow, which results in an aerodynamic

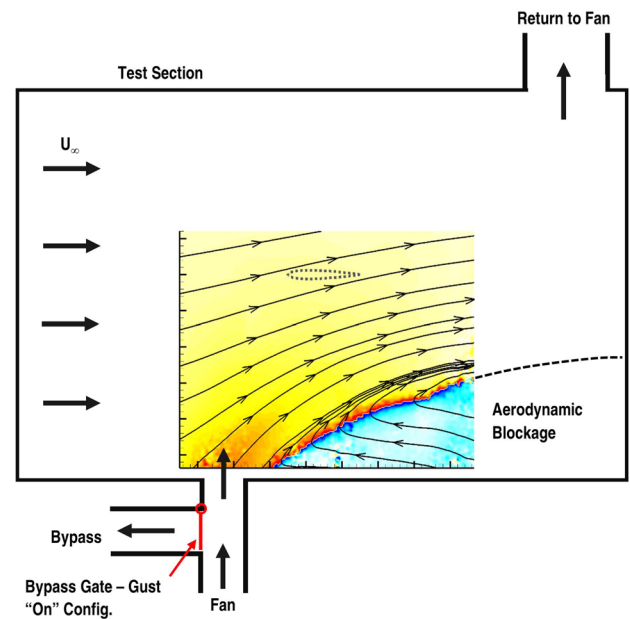


Fig. 1 Schematic of ARGGUS Gust generation mechanism—dashed airfoil representative of test model location

Table 1 Test conditions

Case Name	U_∞	Re_∞	Re_{avg}	Gust Ratio	α_{eff}
GR 0.2, $Re = 12 \times 10^3$	1.5 m/s	12,000	11,600	0.19	11.5°
GR 0.2, $Re = 54.4 \times 10^3$	6.8 m/s	54,400	52,500	0.17	10°
GR 0.3, $Re = 12 \times 10^3$	1.5 m/s	12,000	10,600	0.31	17°

blockage effect in the test region. The incoming freestream flow deflects the jet downstream and some portion of the incoming flow is accelerated upward and over the impinging jet. This results in a region with a gust ratio upward of 25% with minimal freestream speed fluctuations and low turbulence. Flow from the furthest-downstream part of the test section was routed back into the ARGGUS fan, creating a closed-loop system and conserving mass flow in the test section. The ARGGUS was also designed with a bypass loop which allows for the fan to run continually without the jet entering into the test section. This serves to increase gust actuation speed by keeping the gust jet flow momentum high prior to gust actuation. A gate mounted to a rotary actuator directs the flow either into the test section or through the bypass loop. Further discussion of this type of gust generation device was presented by Smith et al. (2018). Gust characterization and some lift interaction data, specifically in Figs. 5, 6, 7, are reproduced from Stutz et al. (2022).

The steady “gust-on” flow generated by the ARGGUS was characterized using Particle Image Velocimetry (PIV) for three gust conditions, given in Table 1. Two of these

gusts developed at a pre-gust freestream Reynolds number of $Re = 12 \times 10^3$ while the third gust condition was tailored to match the lower gust ratio at a higher Reynolds number, $Re = 54.4 \times 10^3$. These Reynolds numbers were calculated based on the 12 cm-chord wings used in the gust-wing interaction experiments. Although work was done to minimize variations in Reynolds number, the gust tended to reduce the freestream velocity near the model by up to $\approx 10\%$. The steady state Reynolds number in the region of the model after the gust is fully developed is given in the table as Re_{avg} . In this work the gusts will be referred to by the freestream Reynolds number and nominal gust ratios, GR 0.2 and GR 0.3, see Table 1. The flow angles generated by the ARGGUS, between $\approx 10^\circ$ to 17° , were similar to those observed in studies of common sUAS operating environments, 5° to 15° (Watkins et al. 2006), and in the updrafts around buildings, up to 45° (Watkins et al. 2019).

The entire opening and closing actuations of the ARGGUS were characterized with PIV. Data were collected at a rate of 10 Hz, with additional characterization of the initial highly-transient development at 100 Hz. Limitations in the storage capacity of the PIV cameras meant that the opening and closing actuations had to be characterized separately. Flow angle, defined as $\alpha_{flow} = \tan^{-1}(v/u)$, was calculated from centerline PIV data as an average of the points within a rectangle with dimensions of 12 cm x 1.44 cm, matching the length and thickness of a NACA 0012 airfoil in the region where a wing model would later be placed for interaction experiments. The flow angle was nominally uniform in this region, as shown by Smith et al. (2018), whose gust generator was the precursor of the ARGGUS. The flow angles from the characterization are shown in Fig. 2 as a function of t^* , where $t^* = U_\infty t/c$. The gust formation was observed

to be nonlinear, making actuation time difficult to define. The GR 0.2 gusts actuate and reach 80% of their steady-gust flow angle in approximately 60 and 80 convective times, Fig. 2a, b, respectively. The GR 0.3 gust reached 80% of its steady-gust flow angle in approximately 37 convective times, Fig. 2c. A short-lived plateau was observed in the flow angle profiles for the two lower Reynolds number gusts. This was caused by the presence of a rotating flow structure convecting downstream near the floor of the test section, which was observed in PIV results (not included in this work) and believed to be created by the opening of the ARGGUS. The flow characterization showed that this structure had completely convected out of the field of view within 5 convective times of the gust actuating on.

The ARGGUS compares favorably with other common gust generation methods. Oscillating vane gust generators typically generate gust ratios in the range of 0.01 to 0.15 (Bicknell and Parker 1972; Brion et al. 2015; Kubo 2018; Lancelot et al. 2015) but those gusts are, by nature, highly transient. The ARGGUS creates gusts of arbitrary length with gust ratios up to 0.3 and 0.2 at Reynolds numbers of 12×10^3 and 54.4×10^3 , respectively. Gust generators in tow tanks often have the ability to create stronger gusts, with ratios above 1.5 (Corkery et al. 2018a, b; Biler and Jones 2020; Perotta and Jones 2017), however the gusts are also inherently very transient given the limited physical width of the jet, which is typically on the order of one to two model chord lengths, limiting the interactions to less than 5 convective times. The closest existing gust generator to the ARGGUS was developed by Olson et al. (2020), which is capable of generating both oscillating gusts and step-function-like gusts of arbitrary length via tip vortices from small vortex generators on the tunnel floor and ceiling. Their gust

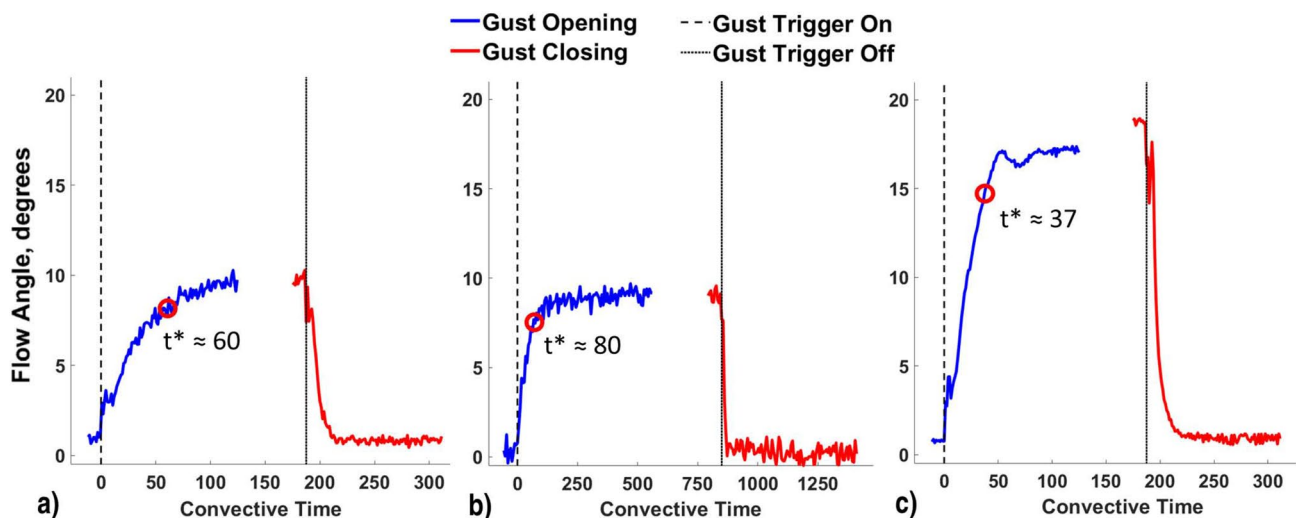


Fig. 2 Flow angle profiles for **a** GR 0.2, $Re = 12 \times 10^3$, **b** GR 0.2, $Re = 54.4 \times 10^3$, and **c** GR 0.3, $Re = 12 \times 10^3$ (Stutz et al. 2022)

generator was able to create a step-function-like gust with a gust ratio of 0.057 in 17 convective times. Although there are inherent issues with extrapolation, if the development rate by Olson et al. was extended to gust ratios of 0.2 and 0.3 then those gusts would develop in 60 convective times and 90 convective times, respectively, which is similar to the development times of the ARGGUS. This suggests that there may be some limit to the rate at which bulk flow angles can be changed when generating gusts by creating aerodynamic disturbances in the flow, but more work would be needed to thoroughly prove this hypothesis. Altogether, the ARGGUS is capable of creating gusts of moderate strength, stronger than most oscillating vane generators but weaker than generators in tow tanks. Importantly, however, it has the ability to create gust interactions of arbitrary lengths of time as opposed to the highly transient gusts from the other two common methods. It is important to note that although the ARGGUS is capable of creating gusts of arbitrary length, a minimum number of convective times are required to reach the peak gust ratio at any setting.

2.2 Force measurements

Force measurements were collected to evaluate the effects of the gust on the lift generated by wings using a 3-component Aerolab Pistol Grip Balance (PGB) (Aerolab 2016). The 12-cm-chord models were mounted to the balance between false walls, spaced 50.8 cm (20 in) apart, with both the gust and wing models spanning the entire distance between the false walls, as shown in Fig. 3. Data were collected using a National Instruments DAQ system through an integrated bridge card. Uncertainty was calculated using the method described in Figliola and Beasley (2012), with

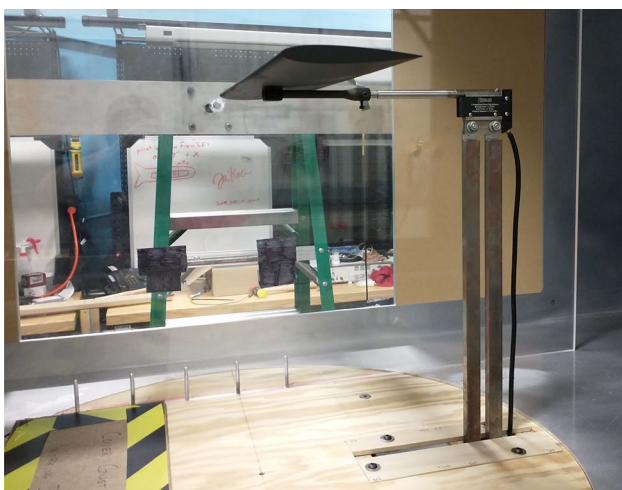


Fig. 3 Model mounted on PGB. *Note:* near-side false wall removed for photograph and safety cover placed over ARGGUS opening (see caution tape)

values typically around ± 0.015 pre-stall and ± 0.03 post-stall. Details on the uncertainty calculations are given in Appendix B.

Force data for the wing-gust interactions was sampled at 500 Hz for 25 seconds, capturing the gust opening, approximately 15 seconds of gust-wing interaction, followed by the gust closing. For the low Reynolds number gusts, this interaction took place over 285 convective times, while for the high Reynolds number case it was 1,300 convective times. Sixty repeated trials were conducted for each gust case, with the airfoil held static at four different angles of attack: -5° , 0° , 5° , and 10° . Ten repeated trials were also collected with the wind tunnel and gust generator fans off to record any vibrations caused by the ARGGUS gate opening and closing. The vibrations caused by the actuation were found to be repeatable, short in comparison to the gust length (roughly 0.4 seconds vs roughly 7 seconds for the gust to develop), and were generally less than 0.07 when converted to C_L . Based on these observations, the opening and closing vibrations were subtracted from the data along with the tare.

2.3 Flow field measurements

The flow fields used in this work were collected using particle image velocimetry (PIV). The high-speed PIV system installed in the MAWT allowed for image pairs to be recorded at a rate of 100 Hz. Two cameras were used to expand the total field of view. Images were collected and processed in LaVision's DaVis 10 software. The flow fields presented in this work are combinations of 25 repeated trials. Uncertainty for the combined flow fields was calculated in DaVis using the methods described and validated in Wienieke (2015) and were found to be between 1.5% to 3% of the freestream speed. Post-processing of the flow fields was done using the method described in Cohn and Koochesfahani (2000) to fit the data onto a regularly spaced grid and calculate vorticity. The models used for the flow field data had the same shape and dimensions as the force data models, however due to the configuration of the MAWT the models were not mounted in the exact same location in the test section. An analysis of the gust characterization flow fields at the model locations showed that the gust was relatively uniform across the model locations and that any discrepancies in flow angle due to model location were small, on the order of $\pm 0.5^\circ$.

3 Results and discussion

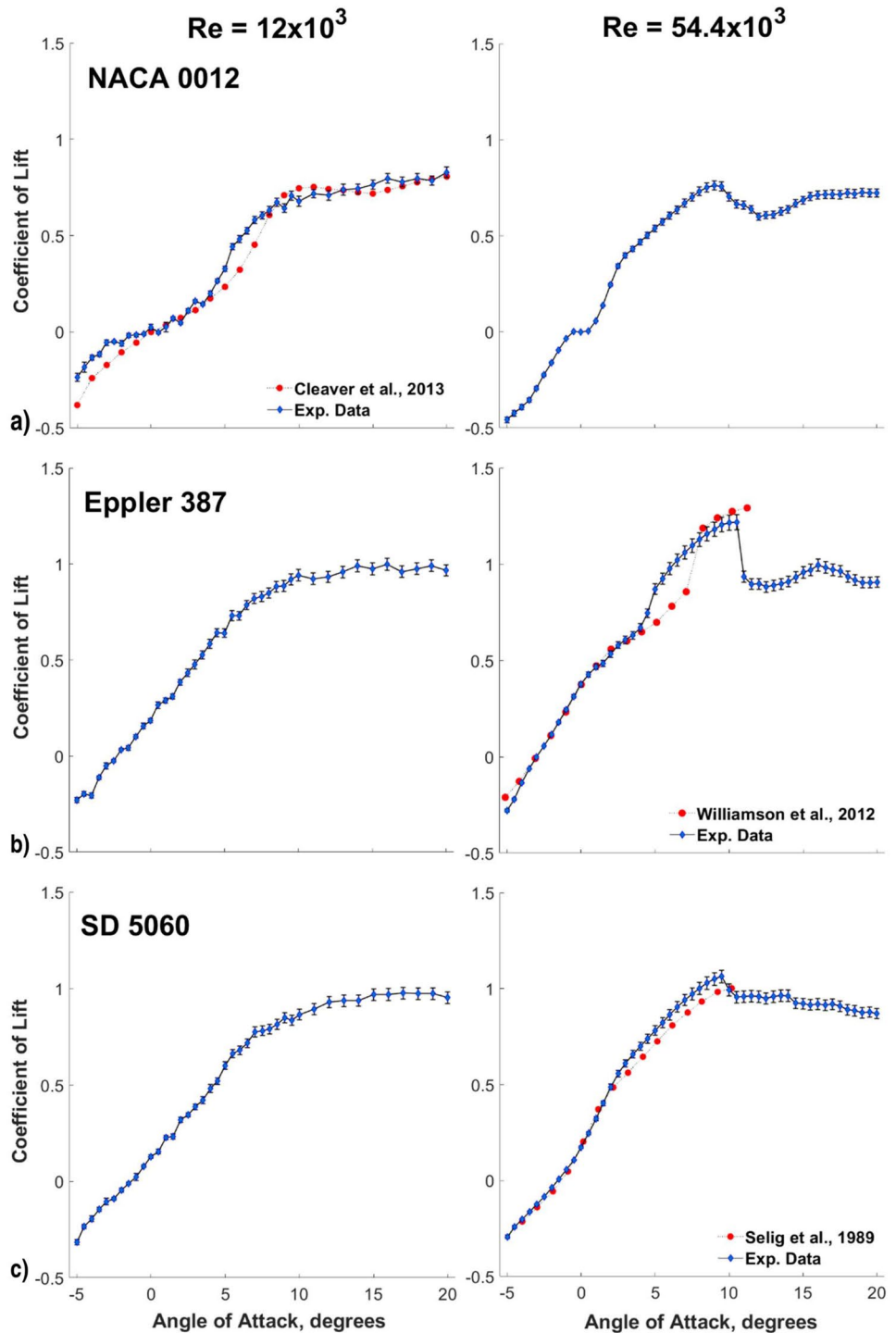
3.1 Static lift curves

Static lift curves were recorded for each airfoil at both Reynolds numbers. It should be noted that there is limited

published airfoil data at these low Reynolds numbers, but the data was compared with other works for validation where possible. The data presented in Fig. 4 are also tabulated in Appendix B to help fill this gap. The NACA 0012 reference data is from Cleaver et al. (2013) and is for $Re = 10 \times 10^3$. The Eppler 387 and the SD 5060 data are from Williamson et al. (2012) and Selig et al. (1989), respectively, and were collected at $Re = 60 \times 10^3$. Static lift data was collected

using at least 3 repeated trials, which proved highly effective for the higher Reynolds number data. Ten repeated trials were conducted at the lower Reynolds number, with outliers removed via a Mahalanobis distance metric. Standard deviation was low for the higher Reynolds number cases and was higher at the lower Reynolds number due to the small forces being measured. Uncertainty was calculated for the collected data and shown as error bars, which are generally on the

Fig. 4 Static lift curves for **a** NACA 0012, **b** Eppler 387, and **c** SD 5060 for $Re = 12 \times 10^3$ (left) and $Re = 54.4 \times 10^3$ (right)



order of size as the data markers used and are most visible in the post-stall region for most cases. More details on the calculation of uncertainty are included in Appendix B.

The static lift curve results had good agreement with the available reference data. Figure 4a also confirms the ability to accurately measure forces at the lower Reynolds number. At low Reynolds number, all three airfoils experienced a soft-stall, where the lift reached a plateau smoothly without the sharp drop associated with airfoil stall at higher Reynolds numbers. The lift data at the higher Reynolds number behaved as expected with nonlinear lift behaviors near $\alpha = 0^\circ$ and a more notable drop in lift post-stall. While there are some minor differences between collected and reference data at higher Reynolds number, several factors may affect those comparisons. These deviations from the reference data are likely due to differences in Reynolds number and turbulence levels (Selig et al. 1989). The turbulence intensity for the reference data was 0.125% for the Eppler 387 (Williamson et al. 2012) and 0.56% for the SD 5060 (Selig et al. 1989) while the MAWT has a freestream turbulence intensity below 0.1% at the higher Reynolds number.

3.2 Calculation of lift coefficient

Figure 5 shows the lift force history of the gust interactions for the NACA 0012. Force data from gust interactions is presented as markers at every 70th data point to allow for differentiation between model angle cases and error bars showing uncertainty for every data point to better illustrate the trends in the data. The uncertainty was calculated using

the same method as the static lift curves. All nine cases in Fig. 5 show that lift reaches a steady condition once the gust is fully developed. Characterization data suggested that the GR 0.2 case creates an effective flow angle of 11.5° at $Re = 12 \times 10^3$ and 10° at $Re = 54.4 \times 10^3$, whereas the GR 0.3, $Re = 12 \times 10^3$ case creates an effective flow angle of 17° . This means that for the NACA 0012, the only cases that do not reach a stalled condition are the model position of $\alpha = -5^\circ$ in the GR 0.2 gusts. Generally the lift profiles all show a rapid increase in lift during gust development, with the steady-gust lift state being reached earlier in the gust development for larger fixed model angles. The $\alpha = -5^\circ$ case in Fig. 5a presents a unique force profile wherein the lift linearly approaches the steady gust condition at a much slower rate, which was not observed for other airfoils or angles tested. The low gust ratio, low Reynolds number, and model orientation may have impacted the tunnel conditions before the gust formed, altering the gust formation behavior somewhat.

There are overshoots above the steady-gust lift values for the lower Reynolds number cases, with the GR 0.3 case, Fig. 5c, showing significantly larger overshoots. Model angles of $\alpha = 0^\circ$ and $\alpha = 5^\circ$ converge to nominally the same condition for all three gust cases, where the flow angles from the characterizations suggest the model should be stalled. The model angle $\alpha = -5^\circ$ case for the GR 0.3 gust should also be stalled once the gust has developed and has a lower lift value, as expected given the lower stalled lift value in the static lift curve for the final effective angle ($\alpha_{\text{eff}} \approx 12^\circ$ as opposed to $\approx 17^\circ$ and $\approx 22^\circ$ for the other two model angles).

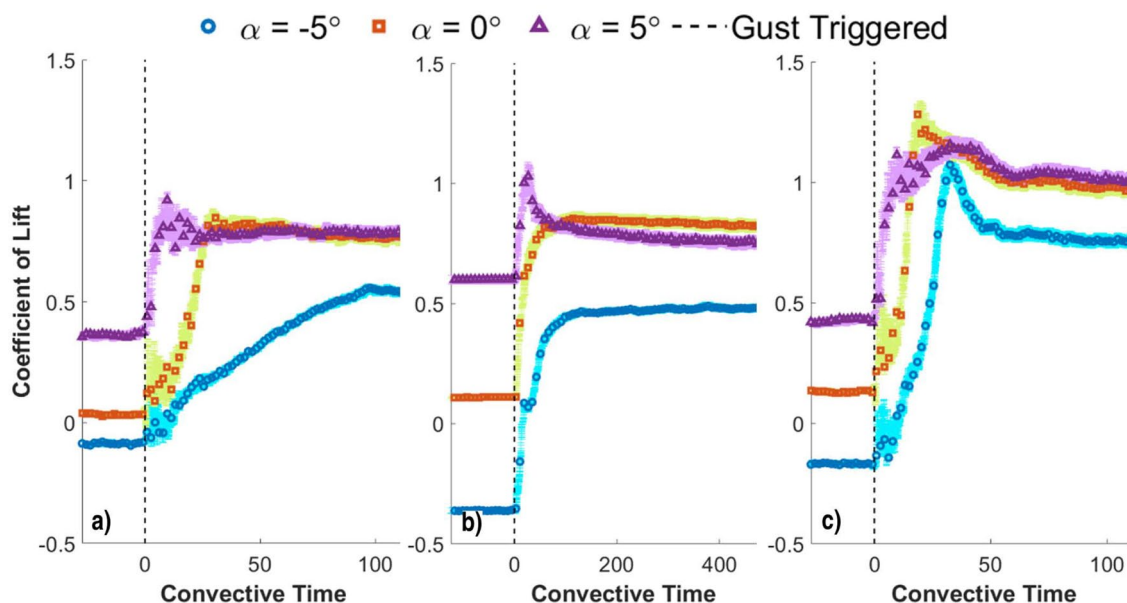


Fig. 5 C_L Calculated using U_∞ for a NACA 0012 entering Gusts **a** GR 0.2, $Re = 12 \times 10^3$, **b** GR 0.2, $Re = 54.4 \times 10^3$, and **c** GR 0.3, $Re = 12 \times 10^3$

The trends in lift data observed in Fig. 5 were notably similar to the flow angle profiles shown in Fig. 2. Figure 6a shows a comparison of the α_{flow} profiles from Fig. 2a and c and the lift from the $\alpha = 0^\circ$ cases from Fig. 5a, c. Figure 6a makes it apparent that the lift response occurs faster than the α_{flow} profile would suggest, along with substantial overshoots in lift. This led to a closer look at how C_L was calculated for gusts generated by this method. The lift coefficients shown in Fig. 5 were calculated using a constant freestream velocity, U_∞ , which is typical for wind tunnel testing. The ARGGUS is known to have a minor effect on the incoming freestream velocity, but it also adds a significant vertical velocity, so the assumption that U_∞ approximates total incoming velocity is insufficient. In a comparable wind tunnel experiment where a model was instead pitched upward and the incoming freestream velocity was changed,

intentionally or due to the model creating increased blockage in the test section, adjustments would be made to accurately normalize lift measurements when calculating the lift coefficient. Burgers and Alexander (2012) investigated cases where normalizing lift with respect to U_∞ may be insufficient and concluded that the typical $\frac{1}{2}\rho v^2$ term in the dynamic pressure should be modified to account for the total kinetic energy required to generate the lift. This simplified to ensuring the total effective velocity was used in the term for fixed-wing cases where a significant vertical velocity component was present. To account for this, lift coefficients for the current study were recalculated using the total velocity, $|V|$, as a function of time from the ARGGUS characterization, shown in Fig. 6b. The method of normalizing lift by $|V|$ for fixed wings proposed by Burgers and Alexander (2012) appears to be well validated by the results of the current study. The

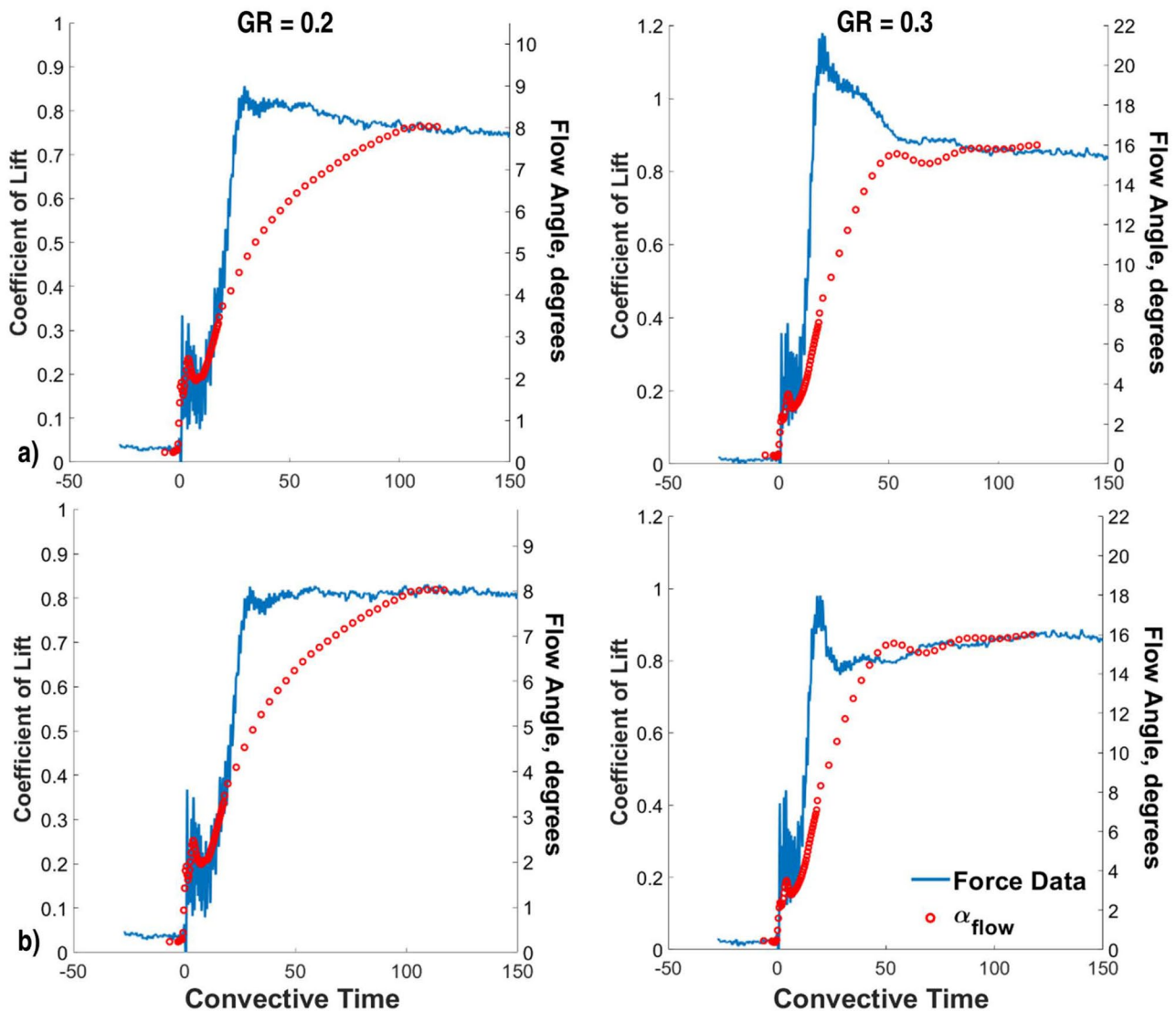


Fig. 6 Comparison of C_L and Gust α_{flow} for GR 0.2 (left) and GR 0.3 (right) Gusts at $Re = 12 \times 10^3$ When C_L is Calculated Using a U_∞ and b $|V|$

lift from both gusts still develops faster than the flow angle would suggest, but there is no longer an overshoot in C_L for the GR 0.2 case and the overshoot is more transient and not as strong in the GR 0.3 case. The lift coefficients presented in the remainder of this work were all calculated using total velocity.

3.3 Force data

The force profiles for all airfoils and gust interactions were recalculated using total velocity and are given in Fig. 7. The overshoot in lift is still present for all three model angles during the GR 0.3 interaction, Fig. 7(c, f, and i), but the overshoots are all smaller and more transient. The overshoots

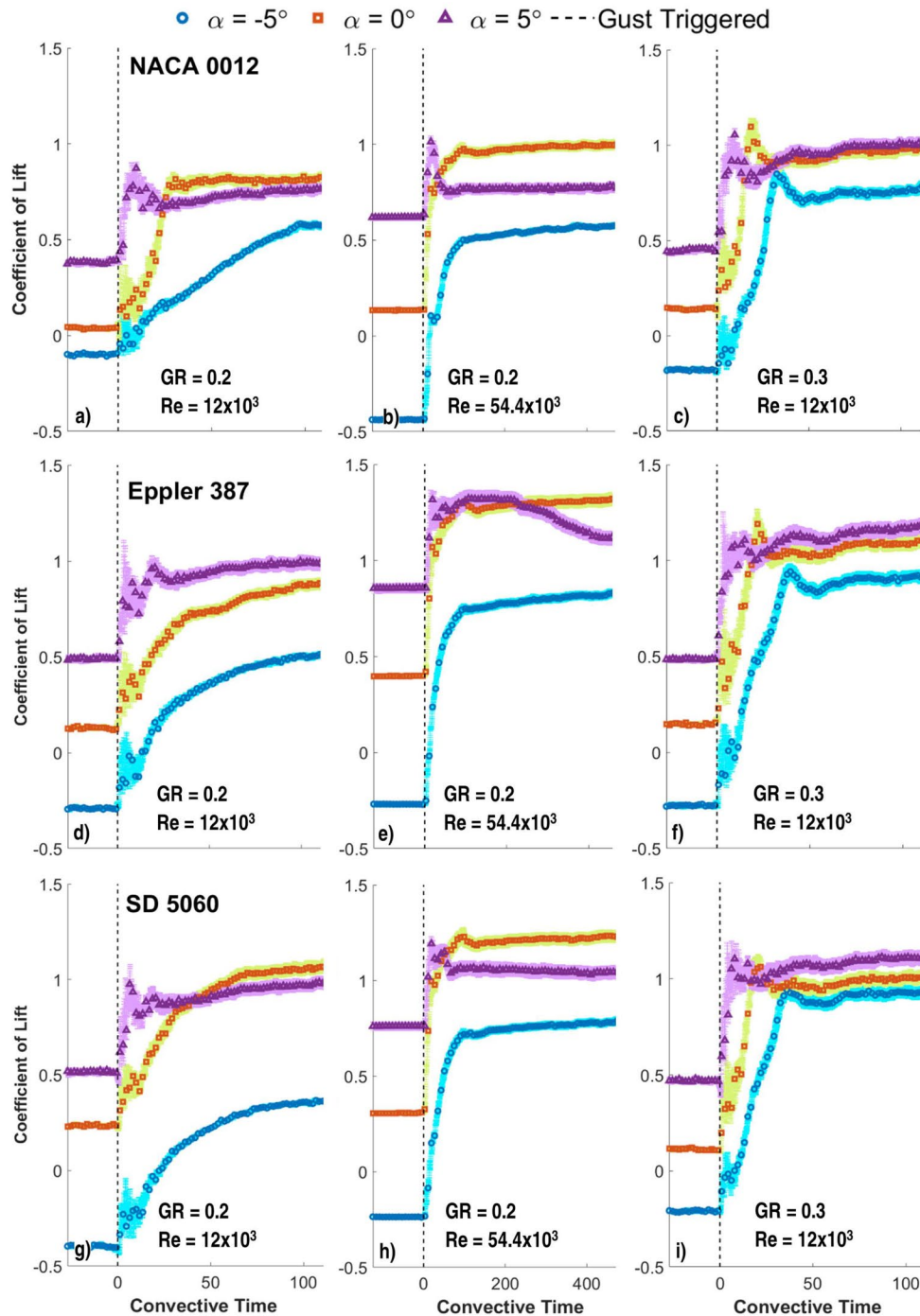


Fig. 7 C_L During Gust interactions using total velocity for **a–c** NACA 0012, **d–f** Eppler 387, and **g–i** SD 5060

seen in the GR 0.2 cases when lift was calculated with U_∞ are no longer present; however, there are still spikes in lift for the model angle of $\alpha = 5^\circ$ for all cases. This spike will be further analyzed in a later section when discussing the flow field data. Aside from the discussed impacts on the overshoot regions, the recalculation of C_L using $|V|$ did not significantly change the trends previously observed in the lift profiles during the gust interactions, although the magnitudes of the lift coefficient were affected in some places as a function of a different velocity in the denominator when calculating C_L . There was still an increase in lift during the gust development which reaches a steady-gust value and the time required to reach that steady state value decreased as model angle increased. The force profiles for the cambered airfoils are given in Fig. 7(d-i) and show that the general trends in lift profiles appear to be consistent across the three airfoils. The $\alpha = 5^\circ$ case for the Eppler 387 experiencing the higher Reynolds number GR 0.2 gust, Fig. 7(e), displayed a unique lift curve during the gust interaction. The raw data of the repeated trials for this case appeared to show the airfoil entering a stalled condition with a steep drop in lift at random times within a window of roughly $t^* = 200$ to $t^* = 500$. The raw data for the model angle of 10° for this case, not shown, also displayed an instability in the pre- and post-gust conditions. This was likely due to the fact that the Eppler 387 airfoil stalls at roughly 10° at this Reynolds number, and small instabilities in the flow likely pushed it to either side of the stall point. A short discussion and data for these cases is given in Appendix A for reference.

3.4 Flow field data

Flow fields were recorded during the gust interactions to better understand the flow physics occurring during the interactions. Key moments during the interaction with the NACA 0012 for a representative case with a lift overshoot, are identified in Fig. 8 along with the corresponding flow fields at those points in time. The first two points in the development, (a) and (b), occur at times in the gust development where the flow angle was below the static stall angle. At these times, the flow around the airfoil began separating near the trailing edge with the reverse flow boundary layer increasing in size as flow angle increased. The separation at (b) can be seen clearly as a region of reverse flow (blue contours) on the airfoil surface in Fig. 9a that extends to the trailing edge of the airfoil. Location (c) marks the beginning of the overshoot in lift, i.e., the location in time where the lift first reaches the steady-gust lift value. The flow angle was approaching the static stall angle of 8° at (c), however Fig. 8c shows that the flow was beginning to reattach at the trailing edge as opposed to continuing to separate. This is clear in the u -velocity at this time, Fig. 9b, where the closed reverse flow region moved upstream of the trailing edge.

The reattachment is clear in Figs. 8d and 9c, the time of peak lift, which occurred at a flow angle well over the static stall angle. Separation began to occur after $t^* = 19.4$, as the flow angle continued to increase. Location (e) is where the lift curve returns to the steady-gust value, marking the end of the overshoot. Separation is clearly present in the flow field corresponding to (e), Fig. 8e, and Fig. 9d shows the recirculation below the separated boundary layer. The characterization showed the flow angle was not completely steady until approximately 80 convective times, however the flow by $t^* \approx 60$ was completely separated and the lift profile had reached a steady condition almost immediately after (e). Location (f) occurs roughly 30 convective times into the steady gust state. The flow fields given for (e) and (f) would suggest that there should be more lift generated at (e), however the measured force profile shows that the lift is roughly the same at both points in time, if not slightly greater at (f). This is caused by the plateau-like stall that the NACA 0012 experiences at such a low Reynolds number. The stall point is approximately 8° , whereas (e) and (f) correspond to flow angles of 12° and 16.6° , respectively. The flow fields, Fig. 8a–f, include a reference arrow to assist in visualizing the flow angle. The angle of the reference vector was not taken from the gust characterization but was calculated from the lower upstream corner of the flow field. Figure 8 appears to show that the reattachment at the trailing edge was the causal mechanism for the overshoot in lift.

The same reattachment behavior was also observed for the NACA 0012 in the $\alpha = -5^\circ$ and $\alpha = 5^\circ$ cases of the GR 0.3 gust, not shown, where the reattachments also aligned with overshoots in lift. The difference between peak lift and steady-gust lift was larger for the $\alpha = 0^\circ$ case than the $\alpha = -5^\circ$ case, and the reattachment was more pronounced. The final flow angle for both cases was well above the static stall angle: 17° for the $\alpha = 0^\circ$ case versus 12° for the $\alpha = -5^\circ$. The main difference between the cases is where in the flow angle development the total effective angle exceeded the static stall angle. This occurred later in the gust development for the $\alpha = -5^\circ$ case, where the rate of change of flow angle development was lower. This suggests that the rate of change of flow angle, $\dot{\alpha}_{\text{flow}}$, is also an important factor in the lift profile during gust interactions. The $\alpha = 5^\circ$ case was different in that the reattachment was not just at the trailing edge but along the entire length of the airfoil. This case will be discussed with the other 5° cases.

The lift profiles for the cambered airfoils experiencing the GR 0.3 gust showed that the cambered airfoils also experienced overshoots above the steady-gust lift, Figs. 7f and i. Although the overshoot was present for both airfoils at a model angle of 0° , the trailing edge reattachment was not. Instead, the flow around and above the airfoils appeared to lag behind the flow angle development upstream of the airfoils. Figure 10 shows the flow field near the time of peak

Fig. 8 Flow field data for important times in gust development for the NACA 0012 experiencing the GR 0.3, $Re = 12 \times 10^3$ Gust at $\alpha = 0^\circ$

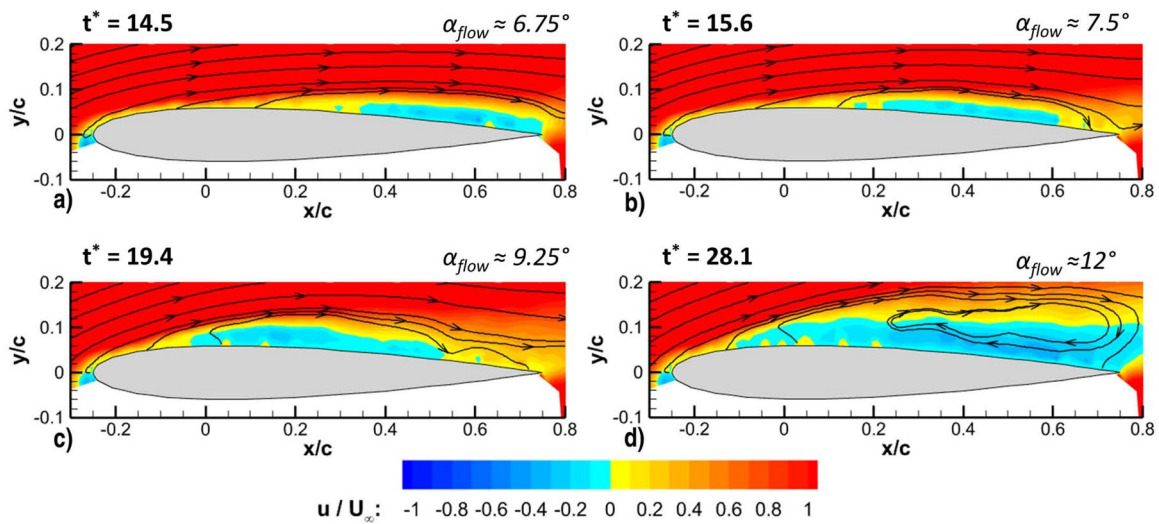
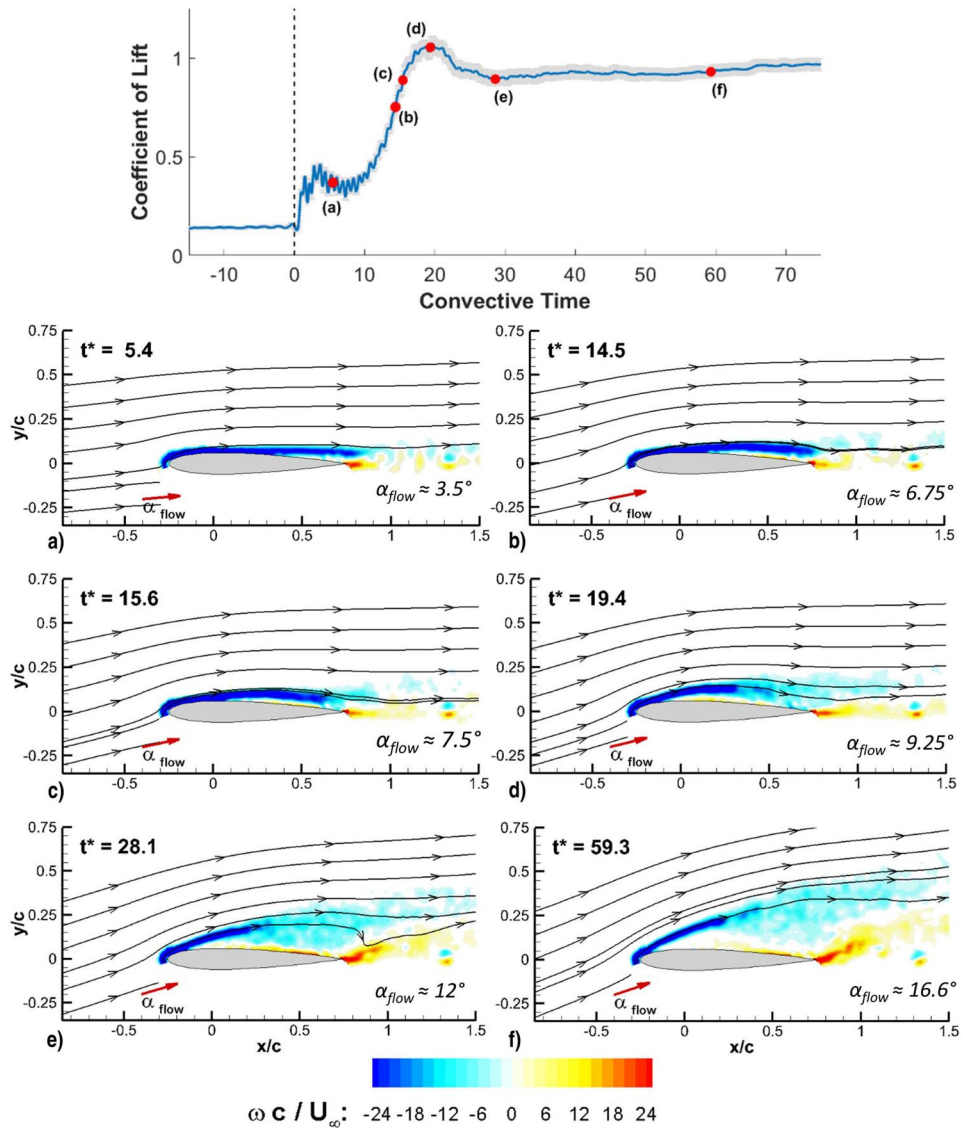


Fig. 9 Reattachment during gust interaction as visualized by u velocity for flow from Fig. 8b–e

lift (left) and after reaching the steady-gust lift (right) for the Eppler 387 (top) and SD 5060 (bottom) airfoils. The flow fields at the time of peak lift showed that the streamlines bent significantly at the vertical plane roughly in line with the leading edge. The streamlines ahead of the leading edge were in line with the flow angle created by the gust development, meanwhile for both airfoils the streamlines near and above the airfoil surface were bent closer to horizontal. Once the overshoot in lift had passed and the steady-gust lift was reached the streamlines near and above the airfoil were deflected to the same angle as the upstream flow angle. This observation suggests that a more broadly accurate description of the gust interaction is that the flow development near the airfoil is delayed. The pre-gust condition for the NACA 0012 at $\alpha = 0^\circ$ is fully attached flow, so the overshoot in lift is associated with reattachment of the flow, whereas the pre-gust condition for the cambered airfoils at $\alpha = 0^\circ$ is partially separated flow, which was present in the flow fields for those airfoils during the overshoot in lift.

A spike in lift was also observed for all airfoils and gust cases for the model angle of 5° . The flow fields showed that the flow reattaches for all of these cases. The reattachment was along the entire length of the NACA 0012 and SD 5060 airfoils, whereas there was a small region of reversed flow remaining near mid-chord for the Eppler 387. A sample of these flow fields during the reattachment is given in Fig. 11. The ubiquity of the reattachment and the early time in the gust development at which it occurred suggested that the

causal mechanism was different from the overshoots seen in the other cases. The model angle of $\alpha = 5^\circ$ was relatively close to the stall angle for all three of the airfoils, which are known to be sensitive to turbulence and other flow disturbances at low Reynolds numbers. The time at which the reattachments and subsequent spikes in lift occurred aligned closely with the short disturbance noted early in the flow angle profiles. Note, however, that the flow disturbance and the reattachments only occurred in the first 5 to 6 convective times after the gust was actuated whereas the spike in the lift profiles typically lasted longer. This is believed to be a function of the time required for the flow to recover from the reattachment and re-separate, which is supported by the fact that some of the lift profiles did not return directly to the steady-gust lift, see Fig. 7c and d, but first dipped below the steady-gust lift due to the separation developing.

An interesting observation was made in the flow field data that was not preempted by the force data, specifically in the $\alpha = -5^\circ$ cases for the cambered airfoils, and most obviously with the SD 5060. The original gust flow characterization showed that the final flow angle for the GR 0.2 gust at that Reynolds number should be 10° ; however, the actual flow angle extracted from the gust interaction flow field was $\approx 9^\circ$. This decrease in flow angle appears to have been due to the presence of the model in the flow. The impact of the cambered airfoils on the flow was present lower in the y/c direction when the airfoils were pitched down. This effect is most likely because of the method of gust generation used by the

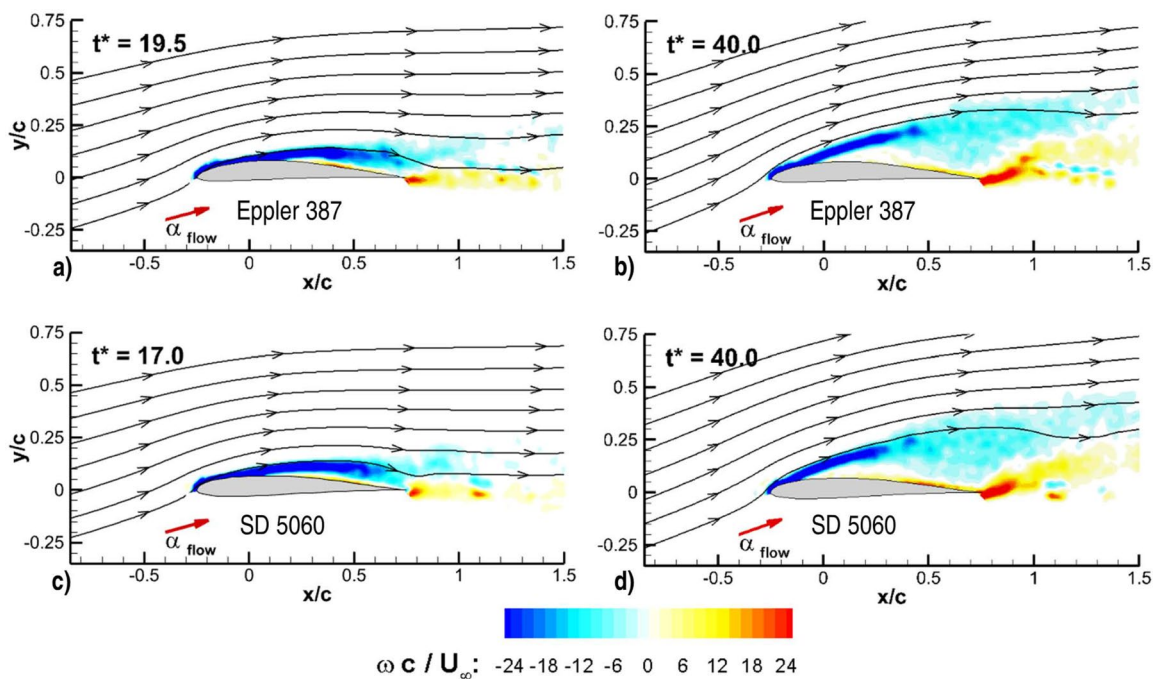


Fig. 10 Flow field data for the Eppler 387 (top) and SD 5060 (bottom) airfoils experiencing the GR 0.3, $Re = 12 \times 10^3$ Gust at $\alpha = 0^\circ$ during overshoot period (left) and after reaching steady-gust lift (right)

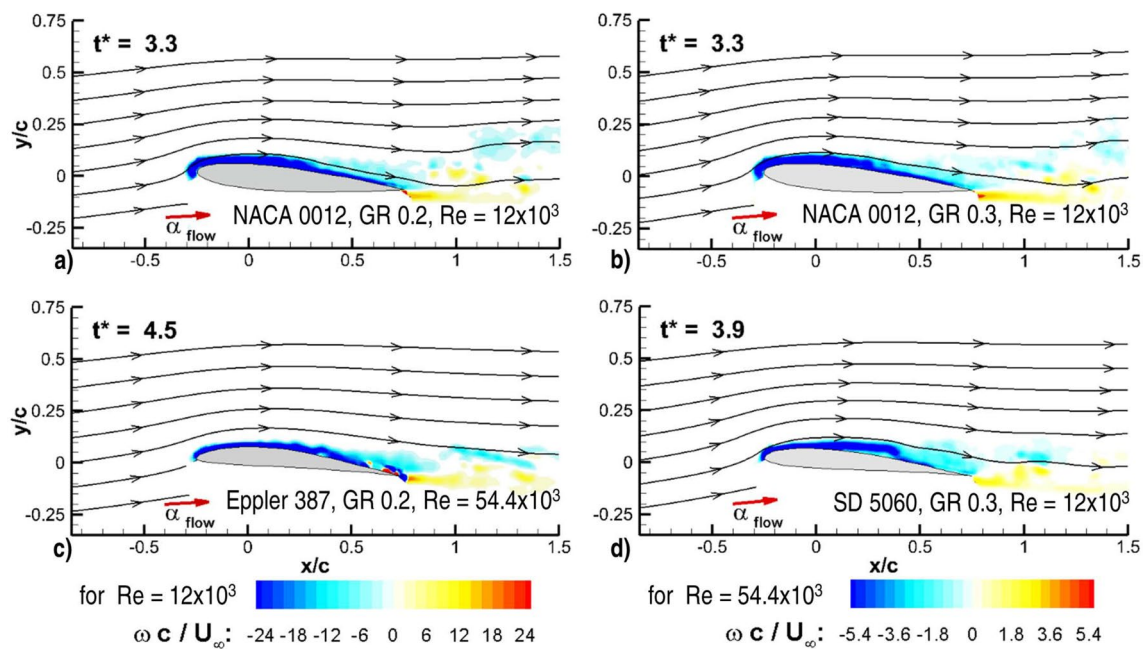


Fig. 11 Examples of sensitivity to disturbances at $\alpha = 5^\circ$ for NACA 0012 (top) and cambered airfoils (bottom) during gust interactions

ARGGUS. Recall that the ARGGUS uses an aerodynamic blockage to create the gust, which may be affected more by cambered wing models. The gust generator by Fernandez et al. (2021) showed the same effect, i.e., the airfoil impacted the gust flow angle by up to 1° .

4 Gust interaction force prediction method

There is an obvious practical desire to be able to predict the lift generated during a gust encounter. Ideally a prediction model should be simple enough that it could easily be integrated into the onboard controller of an sUAS such that the vehicle could predict the change in lift and respond accordingly. Goman and Khrabrov (1994) developed a mathematical model to calculate the lift created during high angle of attack pitching maneuvers, and a modified version of this model has been applied to gusts by Sedky et al. (2020). This model attempts to account for the departures from the static lift curve due to the presence of dynamic effects by considering the angle of attack and the rate of change in the angle of attack, $\dot{\alpha}$ (Goman and Khrabrov 1994). This is done with a general state variable that accounts for the time “lag” between the flow and the dynamic motion (Williams et al. 2017). Significant effort was required to fit this model to the data in this study, which was documented in Stutz et al. (2022).

The similarities in trends shown in Fig. 6b suggested that it may be possible to roughly approximate the lift generated by a gust as a function of change in flow angle. A new

model was developed, called the Flow Angle model (FA model), which used the α_{flow} profiles created by the gusts and applied the corresponding C_L for that angle from the static lift curve for that airfoil at the appropriate freestream Reynolds number. For the cases where the airfoil was not at $\alpha = 0^\circ$ the static angle was added to the α_{flow} created by the gust to determine the total α_{eff} . Applying static lift data, i.e., a $C_L - \alpha$ curve, to analysis of the gust cases requires a rotation to be applied to the static lift and drag, see Eq. 1. Static stall angles of airfoils are typically below 15° and flow angles generated by the gust generator were also below 20° . The generally small values of α_{flow} allows for Eq. 1 to be simplified to Eq. 2 because of the trigonometric functions and small angle approximations. The associated errors from this simplification will be less than 6% for flow angles below 20° . Given that the flow angles tested in this work are below 20° , the small-angle approximation will be used throughout and validated by later results.

One goal of developing a new model was to create a simple model that could easily be applied to different gust interactions. Although the FA model met that requirement, it was not significantly more accurate than the G-K model. Prior applications of the G-K model showed that accounting for dynamic motion, specifically the pitching rate, could potentially improve the accuracy of the FA model. As such, a Rate-Adjusted Flow Angle model (RAFA model) was created to account for this rate of angle change. This was done by adding a rate term, $\tau \dot{\alpha}_{\text{eff}}$, where τ is a time constant and $\dot{\alpha}_{\text{eff}}$ has units of radians per second. The equations for the RAFA model are given as

$$L_{\text{eff}} = \cos(\alpha_{\text{flow}})L_{\text{static}} \Big|_{\alpha=\alpha_{\text{eff}}} + \sin(\alpha_{\text{flow}})D_{\text{static}} \Big|_{\alpha=\alpha_{\text{eff}}}, \quad (1)$$

$$L_{\text{eff}} \approx L_{\text{static}} \Big|_{\alpha=\alpha_{\text{eff}}} \quad \text{for } \alpha_{\text{flow}} \leq 20^\circ, \quad \text{and} \quad (2)$$

$$C_L(\alpha_{\text{eff}}) = \underbrace{\frac{L_{\text{eff}}}{\frac{1}{2}\rho S|V|^2}}_{\text{Base FA Model}} + \underbrace{2.3\dot{\alpha}_{\text{eff}}}_{\text{Rate Term}}, \quad (3)$$

which simplify to the FA model when the rate term is small. The velocity term used in the prediction equations is the total velocity. The importance of using instantaneous total velocity to calculate C_L was discussed in Sect. 3.2. The time constant, τ , was found by minimizing the error between the prediction and collected force data for the GR 0.3, $\alpha = 0^\circ$, NACA 0012 case, which occurred when $\tau = 2.3$ seconds. This value for τ was then applied to all other cases. Although some initial tuning is required for the RAFA model, the satisfactory results over a range of two gust ratios, two Reynolds numbers, and three airfoils suggests that once the time constant is found it operates as a general value and does not require re-tuning for new cases in this range of Reynolds numbers and gust development rates. However, the time constant may require re-tuning if applied far enough outside of the parameters studied in this work. A simulation by Watkins et al. (2019) observed that gust ratios of $GR = 1$ were observed when approaching a building closely in-line with the rooftop, but weaker gusts were more common when flying higher above the building. These effective gusts resulted

in flow angle changes of up to 45° but occurred over many convective lengths of a typical sUAS. For the strongest gust case in Watkins et al. (2019), flow angle rates of 5 to $52^\circ/s$ were observed for vehicles flying at 1.5 and 15 m/s, respectively. The gust ratios in the current work, when approximating flow angle rate changes linearly, had rates of 2.5 to $10^\circ/s$ with an initial freestream velocity of 1.5 m/s. This suggests that the RAFA model is likely to extend well to real-world gusts observed by sUAS. Also note that the prediction models all require static lift curves as inputs, limiting the models to angles where static lift data was collected.

Figure 12 shows the results of the G-K, FA, and RAFA models for the NACA 0012 airfoil experiencing the GR 0.3 gust. The RAFA model captures the majority of the lift profile in the $\alpha = 0^\circ$ case, Fig. 12b, with some underprediction after the overshoot period, whereas the G-K and FA models are not able to predict the overshoot at all. However, the RAFA model prediction is early for the $\alpha = -5^\circ$ case, Fig. 12a. For that angle the G-K and FA models better predict the lift in the early stages of the gust; however, they do not capture the overshoot, which the RAFA model does a better job of. It is important to note that the RAFA model converges to the FA model once the gust has reached a nominally steady state, as the $\dot{\alpha}$ term approaches zero. At $\alpha = 5^\circ$, Fig. 12c, the RAFA model appears to capture the spike in lift, although it does so later in time than it appeared in the measurement. The models could not predict past α_{eff} of 20° ; however, the FA and RAFA models appear to trend toward the measured steady gust lift, whereas the G-K model is trending downward and away from the measured force. The G-K model appears to perform poorly in the steady gust state for all of the angles.

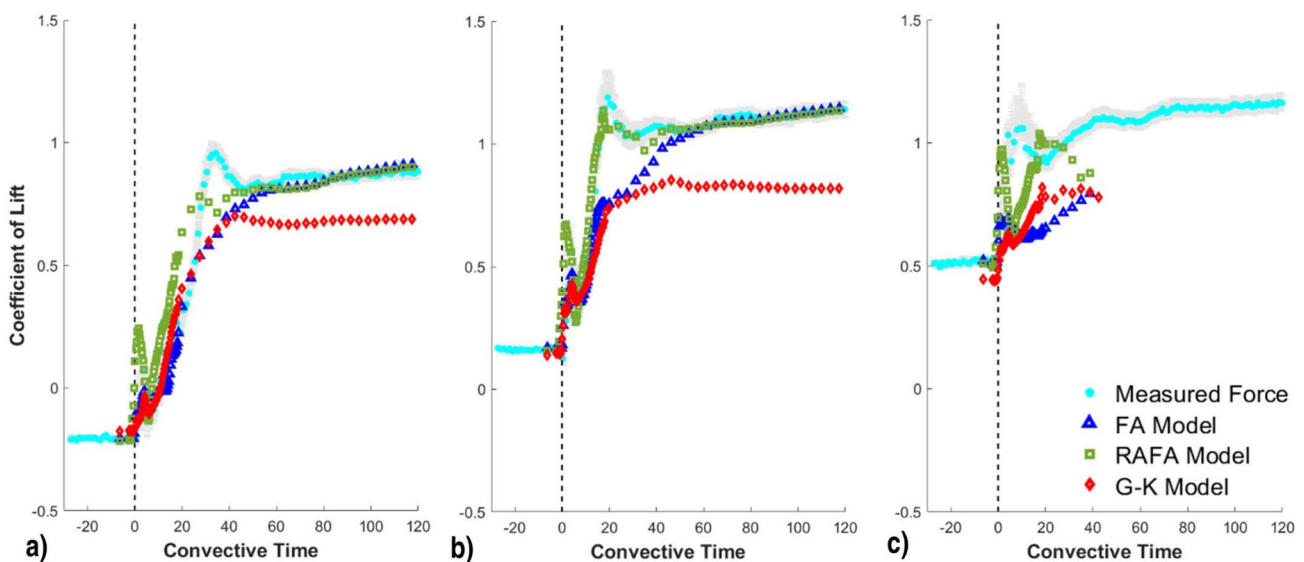


Fig. 12 Prediction of lift for a NACA 0012 entering the GR 0.3 Gust at **a** $\alpha = -5^\circ$, **b** $\alpha = 0^\circ$, and **c** $\alpha = 5^\circ$

The comparison shows that there is little to no benefit to using the G-K method over the FA and RAFA models in terms of prediction accuracy. The G-K and FA models both fail to accurately recreate the overshoot in lift seen in the measured data, and the G-K model under-predicts the lift in the steady gust state. The RAFA model does not perfectly capture the overshoot; however, it does reflect the increase in lift above the steady gust state. There is also what appears to be an overestimation in lift immediately after the gusts are triggered. This was caused by the initial rapid increase in flow angle, see Fig. 2, generated by a transient flow structure formed by the opening of the gust generator. This disturbance in the flow is inherent to the gust formation mechanism and when this was artificially removed from the flow angle characterization, which is more characteristic of a real-world gust that an sUAV might encounter, the sharp overestimations were no longer observed in the model outputs. This work will focus on the RAFA model going forward due to the lack of inherent benefit to the G-K model and the fact that the FA model is not significantly more simple than the RAFA model. However, Fig. 12 does show a way that the FA model could still be useful. The prediction closely matched the measured force in the periods before and after the overshoot, whereas it significantly underpredicted lift during the overshoot period. Applying the FA model to collected sets of force data could highlight the periods of the gust interaction that do not behave as a simple change in flow angle and should be the focus of flow field investigation.

The RAFA model was also applied to the cambered airfoils using the same value for τ . The model performed well in the pre-stall region but typically underpredicted lift once α_{eff} exceeded the static stall angle. This underprediction appeared to be roughly equal to the zero-angle lift for the airfoils at the tested Reynolds numbers. An extra term was included in the C_L calculation in the model which added the zero-angle lift for the airfoil at the appropriate Reynolds number when α_{eff} exceeded the static stall angle, creating the Camber and Rate Adjusted Flow Angle (CRAFA) model. The extra camber-adjusting term has no impact for cases where α_{eff} never exceeds the static stall angle or for symmetric airfoils where the zero-angle lift is zero. The physics to justify the camber term are not currently clear, and that understanding could potentially inform an even more accurate model. It is likely that the camber correction is required because of the impact that the presence of the cambered airfoils have on the gust flow. This would mean that the CRAFA model is only suitable for experimental gust studies where this impact occurs, and that the RAFA model is more appropriate for naturally occurring gusts and generated gusts that are not constrained in the way that gusts from the ARGUS are.

However, the stated goal of the current work was to create a simple prediction model that was more accurate than the current standard and from that perspective the addition of the camber term is sufficient. The direct addition of the cambered term was deemed acceptable to maintain simplicity, however the camber term could be added in a smoothed fashion if the model was to be applied in an experimental setting as part of a control response. The final equation for the CRAFA model is

$$C_L(\alpha_{\text{eff}}) = \underbrace{\frac{L_{\text{eff}}}{\frac{1}{2}\rho S|V|^2}}_{\text{Base FA Model}} + \underbrace{2.3\dot{\alpha}_{\text{eff}}}_{\text{Rate Term}} + \underbrace{\text{Corr}_{\text{camber}}}_{\text{Camber Term}}, \quad (4)$$

where $\text{Corr}_{\text{camber}}$

$$= \begin{cases} 0 & \text{if } \alpha_{\text{eff}} < \alpha_{\text{stall,static}} \\ C_{L_{\text{static}}} \Big|_{\alpha=0} & \text{if } \alpha_{\text{eff}} \geq \alpha_{\text{stall,static}} \end{cases}. \quad (5)$$

Sample results from the RAFA and CRAFA models are shown in Figs. 13 thru 15 for the Eppler 387 and SD 5060 airfoils. These figures, along with Fig. 12, show that the accuracy of the CRAFA model is consistent across different airfoils and Reynolds numbers. The addition of the camber term makes the new model highly accurate for some of the camber cases. The results from the model for both cambered airfoils experiencing the GR 0.3 gust at $\alpha = 0^\circ$, Figs. 13b and 14b, lay almost entirely within the uncertainty of the measured data. The case shown in Fig. 15c is almost an exact replication of the measured forces. Note that there is no difference between the RAFA and CRAFA model outputs in Figs. 14c and 15a, b. This is because the effective angle for the GR 0.2 gusts did not exceed the static stall angle for those cases. An interesting point of note is the over prediction of lift seen in Figs. 13a and 14a for the CRAFA model. This is likely due to a change in the gust flow caused by the presence of the cambered airfoils in the flow, which was also observed in the flow fields for those cases. With that in mind, it may be more accurate to describe the predictions for these two cases as accurate to the gust characterization, but the presence of the airfoil has caused the actual gust performance, and therefore the measured forces, to deviate from the characterization.

The accuracy of the predictions is best evaluated by looking at three distinct periods of the gust: the initial gust development, the period of overshoot, and the steady gust state. The total average error in C_L for all 25 gust-wing

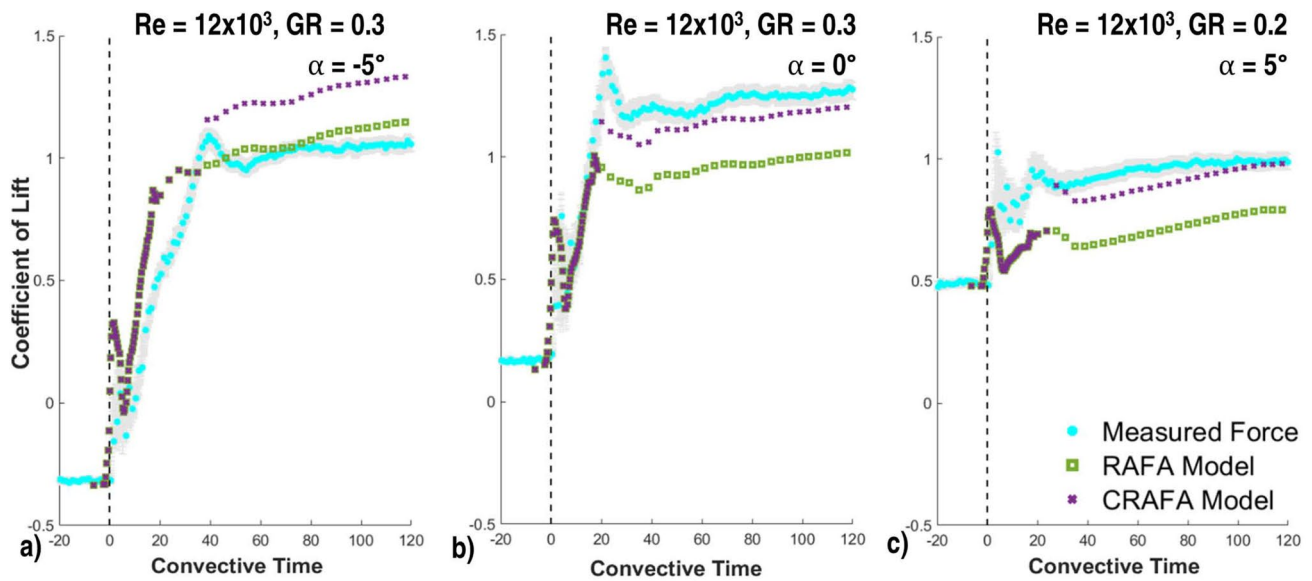


Fig. 13 Sample results from RAFA and CRAFA Models for the Eppler 387 at $Re = 12 \times 10^3$

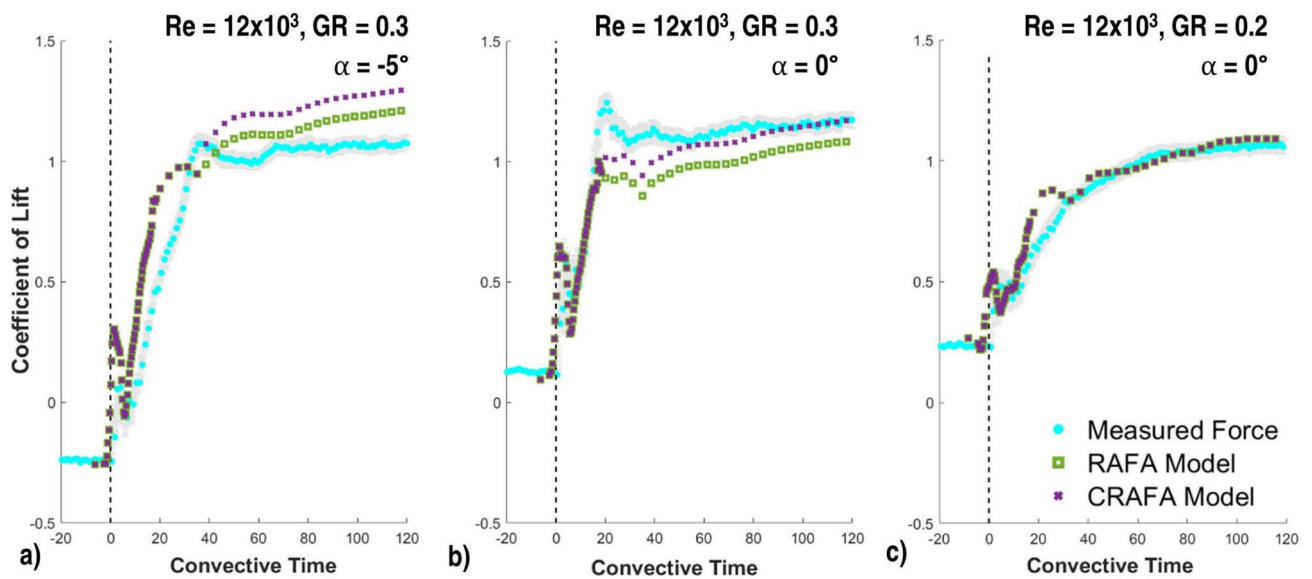


Fig. 14 Sample results from RAFA and CRAFA Models for the SD 5060 at $Re = 12 \times 10^3$

interaction cases (i.e. all three airfoils at all three angles for the three gust cases, minus the two discussed outlier cases, one each for the NACA 0012 and Eppler 387) for the FA, RAFA, and CRAFA models are given in Table 2 in C_L and as factors of the average uncertainty of the measured forces, where $\overline{u_{C_L}} = 0.021$. The general accuracy of the FA model in the early gust development is confirmed by the minimal impact on the accuracy by adding the rate and camber terms. The rate adjustment appears to have

increased accuracy during the overshoot period, with the decrease in error likely driven largely by the accuracy of the NACA 0012 results. The addition of the camber term increases the accuracy when modeling the cambered airfoils, decreasing the error in the overshoot region by almost 50% compared to the FA model and 30% compared to the RAFA model. The camber term also corrects the consistent underprediction of lift at the steady gust state and therefore is more accurate than the other two

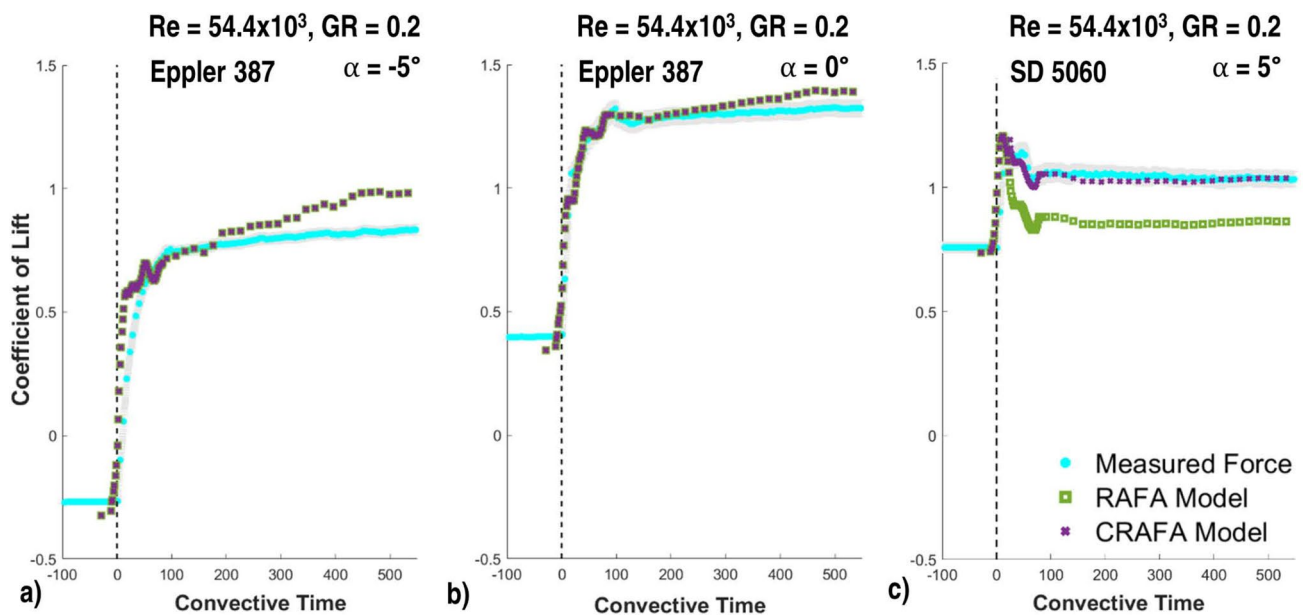


Fig. 15 Sample results from RAFA and CRAFA Models for the Cambered Airfoils at $Re = 54.4 \times 10^3$

Table 2 Gust model errors

	FA Model $\overline{e_{C_L}}$	RAFA Model $\overline{e_{C_L}}$	CRAFA Model $\overline{e_{C_L}}$
Early Gust	0.176 ($\approx 8\overline{u_{C_L}}$)	0.165 ($\approx 8\overline{u_{C_L}}$)	0.152 ($\approx 7\overline{u_{C_L}}$)
Overshoot Region	0.193 ($\approx 9\overline{u_{C_L}}$)	0.153 ($\approx 7\overline{u_{C_L}}$)	0.114 ($\approx 5\overline{u_{C_L}}$)
Steady Gust	0.119 ($\approx 6\overline{u_{C_L}}$)	0.118 ($\approx 6\overline{u_{C_L}}$)	0.099 ($\approx 5\overline{u_{C_L}}$)

models in that time region as well. The accuracy of the RAFA and CRAFA models across the parameters in this work suggests the models, with the current time constant value, should be generally applicable within the range of Reynolds numbers and gust ratios herein, however τ may need to be re-evaluated for data sets outside of that range. If the current value of τ is found to not be generally applicable, the additional work required for other data sets may also provide a general relationship for τ based on flow conditions.

The simplicity of the RAFA and CRAFA models, paired with the accuracy, make them excellent candidates for future use. The only necessary inputs for the models are the static lift curve and the velocity and flow angle information at any given time. The models could easily be integrated into the control system of any sUAS that is capable of measuring its velocity and the angle of incoming flow with only a simple equation and a small set of static lift curves that cover its expected flight envelope.

5 Conclusions

The ARGGUS system has created the opportunity to study gust interactions over longer time scales. The force profiles during gust interactions showed that the generated lift was steady once the gust reached a steady state, and that there were overshoots in lift above the steady-gust lift for certain cases. Investigation of the flow fields indicated that the overshoots in lift corresponded with a delayed development of the flow angle near and above the airfoil surface. Analysis of the forces generated by the gusts demonstrated that it was significantly more accurate to normalize the lift coefficient by the total velocity, as opposed to the freestream velocity. The collected force and flow field data also showed that the gusts generally acted as changes in incoming flow angle and that the rate of change of flow angle was also important in determining the lift profile. This allowed for the creation a simple force prediction model, the CRAFA model, that applied the static lift curve for a given airfoil to the α_{flow} profile created by the gust. The CRAFA model was able to accurately predict the lift during the gust interaction by accounting for the rate of change of α_{eff} and the camber of the airfoil. This model relies only on static lift data and a single time constant (τ), and was shown to be simpler and more accurate for a range of airfoils and for Reynolds number from 12×10^3 to 54.4×10^3 than the modified version of the Goman–Khrabrov model that is currently in use. The new CRAFA model may give future control systems the ability to proactively predict and account for the changes in lift due to gust encounters.

Appendix A Unique stall instability of the Eppler 387 during gust encounters

Investigation of the collected lift force data for the Eppler 387 at two angles, $\alpha = 5^\circ$ and 10° , during the GR 0.2 interaction at $Re = 54.4 \times 10^3$ demonstrated interesting instabilities. The $\alpha = 5^\circ$ case, Fig. 16a, appears to show the airfoil experiencing a stall-like drop in lift at random times within a window of ≈ 200 convective times, all after the steady-gust state has been reached. This instability was not seen in any other cases in this work. This data suggests that the airfoil was likely very close to the static stall angle during this time and thus a stall event was triggered by some instability in the flow, likely freestream turbulence. The $\alpha = 10^\circ$ case, Fig. 16b, shows a bi-stability in the pre- and post-gust states. Likely because the model angle of 10° is very close to the static stall angle for the Eppler 387 at this Reynolds number. This bi-stability serves as a good illustrator of the sensitivity of this airfoil to flow disturbances near stall.

Appendix B method for calculating uncertainty

The method for calculating the uncertainty of the measured force data was taken from Figliola and Beasley (2012). This method accounts for the random uncertainty, s , and bias uncertainty, b , inherent in data collection. The random uncertainty is a measure quantifying the variability of each input, whereas the bias uncertainty covers measurement accuracy and error. The equations used on the data from the force balance are given below, where Eqs. 6–8 are applied to the normal and axial force measurements. The outputs of Eqs. 7 and 8 are used in 10 and 11 with subscripts denoting the normal and axial directions. The random and bias uncertainty values used in the equations, along with how they were determined, are given in Table 3. Note that there is assumed to be no random uncertainty for air density, model planform area, or model angle as these values should not fluctuate. The measured static lift curves and the corresponding uncertainty values are tabulated in Tables 4 and 5.

Fig. 16 Examples of Eppler 387’s sensitivity to flow angle for GR 0.2 at $Re = 54.4 \times 10^3$ at model angles of **a** 5° and **b** 10° . Note these C_L values are calculated with U_∞

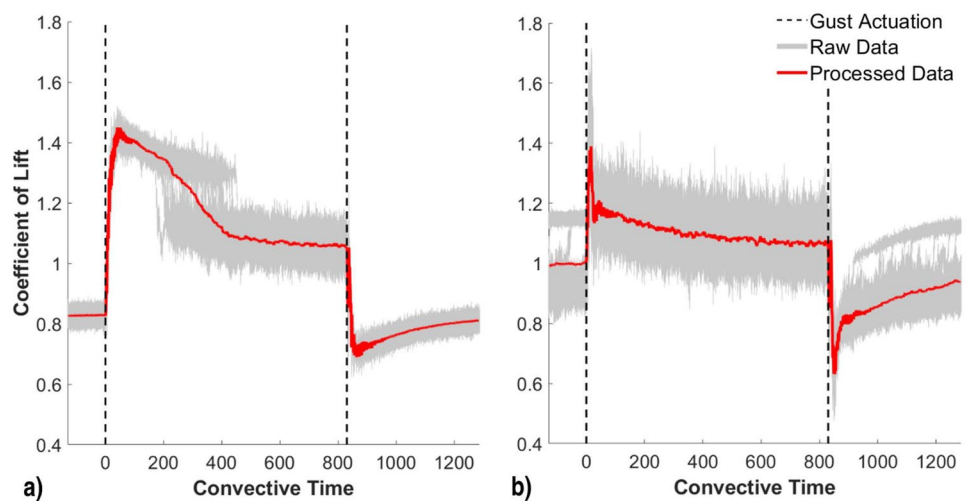


Table 3 Uncertainty calculation inputs

Variable	s_x	s_x Rationale	b_x	b_x Rationale
ρ [kg/m ³]	0	N/A	± 0.01	$\Delta\rho$ for $\Delta T_{lab} \pm 2.5^\circ C$
v [m/s]	$\pm 0.01v$	Internal ARL MAWT Calibration	$\pm 0.01v$	Internal ARL MAWT Calibration
S [m ²]	0	N/A	$\pm 1.57 \times 10^{-7}$	0.04 cm [1/64 in] error in chord and span
F_N [N]	$\pm \sigma_{F_N} / \sqrt{N_{F_N}}$	2012)	$\pm 0.009653 F_N$	2016)
F_A [N]	$\pm \sigma_{F_A} / \sqrt{N_{F_A}}$	2012)	$\pm 0.02371 F_A$	2016)
α [°]	0	N/A	± 0.01	2012)

Table 4 Tabulated static lift coefficients at $Re=12 \times 10^3$

α (°)	NACA 0012		Eppler 387		SD 5060	
	C_L	$\pm u_{C_L}$	C_L	$\pm u_{C_L}$	C_L	$\pm u_{C_L}$
-5	-0.237	0.020	-0.229	0.014	-0.315	0.013
-4.5	-0.185	0.026	-0.196	0.013	-0.233	0.011
-4	-0.134	0.013	-0.206	0.014	-0.194	0.014
-3.5	-0.117	0.012	-0.111	0.009	-0.144	0.010
-3	-0.057	0.015	-0.051	0.015	-0.104	0.018
-2.5	-0.051	0.007	-0.025	0.007	-0.090	0.008
-2	-0.060	0.014	0.034	0.006	-0.046	0.011
-1.5	-0.019	0.010	0.043	0.012	-0.010	0.007
-1	-0.018	0.009	0.102	0.009	0.023	0.017
-0.5	-0.010	0.005	0.158	0.014	0.078	0.006
0	0.024	0.015	0.185	0.011	0.129	0.009
0.5	-0.004	0.008	0.265	0.016	0.155	0.011
1	0.024	0.025	0.290	0.014	0.227	0.010
1.5	0.069	0.010	0.312	0.013	0.233	0.013
2	0.046	0.007	0.384	0.014	0.319	0.014
2.5	0.110	0.010	0.432	0.020	0.345	0.011
3	0.159	0.007	0.477	0.024	0.386	0.014
3.5	0.144	0.008	0.526	0.022	0.421	0.017
4	0.199	0.013	0.584	0.023	0.482	0.020
4.5	0.265	0.009	0.642	0.021	0.520	0.017
5	0.327	0.013	0.640	0.022	0.600	0.020
5.5	0.442	0.015	0.730	0.025	0.663	0.021
6	0.481	0.018	0.730	0.023	0.680	0.022
6.5	0.526	0.017	0.786	0.024	0.716	0.022
7	0.582	0.018	0.820	0.026	0.775	0.025
7.5	0.604	0.019	0.830	0.027	0.781	0.024
8	0.630	0.023	0.849	0.027	0.790	0.025
8.5	0.673	0.022	0.882	0.028	0.814	0.025
9	0.642	0.023	0.886	0.028	0.848	0.026
9.5	0.708	0.024	0.920	0.029	0.836	0.027
10	0.679	0.026	0.942	0.029	0.866	0.028
11	0.718	0.022	0.923	0.030	0.894	0.029
12	0.709	0.025	0.933	0.029	0.931	0.029
13	0.739	0.029	0.957	0.030	0.936	0.029
14	0.742	0.024	0.991	0.031	0.938	0.029
15	0.765	0.023	0.975	0.032	0.968	0.031
16	0.797	0.024	0.999	0.032	0.969	0.031
17	0.779	0.025	0.960	0.030	0.976	0.030
18	0.797	0.025	0.975	0.030	0.974	0.030
19	0.786	0.024	0.991	0.031	0.974	0.030
20	0.829	0.027	0.967	0.030	0.953	0.030

Table 5 Tabulated static lift coefficients at $Re=54.4 \times 10^3$

α (°)	NACA 0012		Eppler 387		SD 5060	
	C_L	$\pm u_{C_L}$	C_L	$\pm u_{C_L}$	C_L	$\pm u_{C_L}$
-5	-0.458	0.014	-0.278	0.009	-0.293	0.009
-4.5	-0.424	0.013	-0.220	0.007	-0.243	0.007
-4	-0.391	0.012	-0.135	0.004	-0.203	0.006
-3.5	-0.354	0.011	-0.062	0.002	-0.164	0.005
-3	-0.293	0.009	-0.000	0.000	-0.124	0.004
-2.5	-0.224	0.007	0.056	0.002	-0.085	0.003
-2	-0.160	0.005	0.118	0.004	-0.037	0.001
-1.5	-0.095	0.003	0.179	0.006	0.008	0.000
-1	-0.036	0.001	0.246	0.008	0.057	0.002
-0.5	0.002	0.000	0.315	0.010	0.106	0.003
0	-0.000	0.000	0.377	0.012	0.174	0.005
0.5	0.005	0.000	0.427	0.013	0.245	0.008
1	0.056	0.002	0.467	0.014	0.322	0.010
1.5	0.138	0.004	0.484	0.015	0.402	0.012
2	0.246	0.008	0.533	0.017	0.488	0.015
2.5	0.342	0.011	0.580	0.018	0.557	0.017
3	0.397	0.012	0.606	0.019	0.611	0.019
3.5	0.431	0.013	0.630	0.020	0.658	0.020
4	0.467	0.014	0.671	0.021	0.700	0.022
4.5	0.503	0.016	0.745	0.023	0.739	0.023
5	0.538	0.017	0.870	0.027	0.782	0.024
5.5	0.572	0.018	0.925	0.029	0.822	0.026
6	0.605	0.019	0.977	0.031	0.864	0.027
6.5	0.636	0.020	1.022	0.032	0.904	0.028
7	0.671	0.021	1.061	0.033	0.941	0.029
7.5	0.702	0.022	1.097	0.034	0.972	0.030
8	0.732	0.023	1.129	0.036	1.000	0.031
8.5	0.752	0.023	1.157	0.037	1.029	0.032
9	0.761	0.024	1.182	0.037	1.049	0.033
9.5	0.756	0.023	1.206	0.038	1.063	0.034
10	0.704	0.022	1.216	0.039	0.993	0.031
10.5	0.666	0.020	1.218	0.039	0.955	0.030
11	0.660	0.020	0.936	0.029	0.958	0.030
11.5	0.638	0.019	0.896	0.028	0.960	0.030
12	0.600	0.018	0.898	0.028	0.958	0.030
12.5	0.607	0.018	0.882	0.027	0.949	0.029
13	0.610	0.018	0.890	0.028	0.958	0.030
13.5	0.627	0.019	0.897	0.028	0.963	0.030
14	0.638	0.019	0.910	0.028	0.963	0.030
14.5	0.669	0.020	0.932	0.029	0.923	0.028
15	0.685	0.021	0.958	0.030	0.921	0.028
15.5	0.704	0.021	0.970	0.030	0.915	0.028
16	0.713	0.022	0.996	0.031	0.919	0.028
16.5	0.714	0.022	0.983	0.030	0.913	0.028
17	0.716	0.022	0.972	0.030	0.918	0.028
17.5	0.714	0.021	0.964	0.030	0.908	0.028
18	0.722	0.022	0.934	0.029	0.889	0.027
18.5	0.719	0.022	0.918	0.028	0.885	0.027
19	0.725	0.022	0.904	0.028	0.874	0.027

Table 5 (continued)

α (°)	NACA 0012		Eppler 387		SD 5060	
	C_L	$\pm u_{C_L}$	C_L	$\pm u_{C_L}$	C_L	$\pm u_{C_L}$
19.5	0.723	0.022	0.905	0.028	0.877	0.027
20	0.723	0.022	0.907	0.028	0.869	0.027

$$C_F = \frac{F}{\frac{1}{2}\rho|V|^2S}, \quad \text{where } F = \begin{cases} N, & \text{Normal Force} \\ A, & \text{Axial Force} \end{cases} \quad (6)$$

$$s_R = \sqrt{\left[\frac{\partial C_F}{\partial F} s_F\right]^2 + \left[\frac{\partial C_F}{\partial \rho} s_\rho\right]^2 + \left[\frac{\partial C_F}{\partial |V|} s_{|V|}\right]^2 + \left[\frac{\partial C_F}{\partial S} s_S\right]^2} \quad (7)$$

$$b_R = \sqrt{\left[\frac{\partial C_F}{\partial F} b_F\right]^2 + \left[\frac{\partial C_F}{\partial \rho} b_\rho\right]^2 + \left[\frac{\partial C_F}{\partial |V|} b_{|V|}\right]^2 + \left[\frac{\partial C_F}{\partial S} b_S\right]^2} \quad (8)$$

$$C_L = C_N \cos \alpha + C_A \sin \alpha \quad (9)$$

$$s_L = \sqrt{\left[\frac{\partial C_L}{\partial C_N} s_{R_N}\right]^2 + \left[\frac{\partial C_L}{\partial C_A} s_{R_A}\right]^2 + \left[\frac{\partial C_L}{\partial \alpha} s_\alpha\right]^2} \quad (10)$$

$$b_L = \sqrt{\left[\frac{\partial C_L}{\partial C_N} b_{R_N}\right]^2 + \left[\frac{\partial C_L}{\partial C_A} b_{R_A}\right]^2 + \left[\frac{\partial C_L}{\partial \alpha} b_\alpha\right]^2} \quad (11)$$

$$u_{C_L} = \pm \sqrt{s_L^2 + b_L^2} \quad (12)$$

Acknowledgements The authors would like to thank Dr. Todd Henry for 3-D printing the models used in this work and Mr. David Gondol for his help in fabricating critical components of the experimental setup.

Funding: Research was sponsored by the Army Research Laboratory and was accomplished under Cooperative Agreement Number W911NF-19-2-0197. The views and conclusions contained in this document are those of the authors and should not be interpreted as representing the official policies, either expressed or implied, of the Army Research Laboratory or the U.S. Government. The U.S. Government is authorized to reproduce and distribute reprints for Government purposes notwithstanding any copyright notation herein.

References

- Aerolab (2012) ARL microsystems aeromechanics wind tunnel owner's/operator's manual. Aerolab, 8291 Patuxent Range Rd, Jessup, Maryland 20794 USA
- Aerolab (2016) US Army Research Lab Sting Balance Calibration Report. Aerolab, 8291 Patuxent Range Rd, Jessup, Maryland 20794 USA
- Bicknell J, Parker A (1972) A wind-tunnel stream oscillation apparatus. *J. Aircraft* 9(6):446–447. <https://doi.org/10.2514/3.59011>
- Biler H, Jones AR (2020) Force predictions during transverse and vortex gust encounters. Tech. Rep. STO-TR-AVT-282, NATO Science and Technology Organization
- Bohrer G, Brandes D, Mandel JT et al (2012) Estimating updraft velocity components over large spatial scales: contrasting migration strategies of golden eagles and turkey vultures. *Ecol Lett* 15:96–103. <https://doi.org/10.1111/j.1461-0248.2011.01713.x>
- Brion V, Lepage A, Amosse Y et al (2015) Generation of vertical gusts in a transonic wind tunnel. *Exp Fluids* 56:145. <https://doi.org/10.1007/s00348-015-2016-5>
- Buell DA (1969) An experimental investigation of the velocity fluctuations behind oscillating vanes. Tech rep, National Aeronautics and Space Administration
- Burgers P, Alexander DE (2012) Normalized lift: An energy interpretation of the lift coefficient simplifies comparisons of the lifting ability of rotating and flapping surfaces. *PLoS ONE* 7(5). <https://doi.org/10.1371/journal.pone.0036732>
- Cleaver DJ, Wang Z, Gursul I (2013) Investigation of high-lift mechanisms for a flat-plate airfoil undergoing small-amplitude plunging oscillations. *AIAA J* 51(4):968–980. <https://doi.org/10.2514/1.J052213>
- Cohn RK, Koochesfahani MM (2000) The accuracy of remapping irregularly spaced velocity data onto a regular grid and the computation of vorticity. *Exp Fluids* 29:S61–S69. <https://doi.org/10.1007/S003480070008>
- Corkery S, Babinsky H, Harvey J (2018) On the development and early observations from a towing tank-based transverse wing-gust encounter test rig. *Exp Fluids* 59:135. <https://doi.org/10.1007/s00348-018-2586-0>
- Corkery S, Babinsky H, Harvey J (2018b) Response of a flat plate wing to a transverse gust at low reynolds numbers. In: *AIAA SciTech Forum*, Kissimmee, FL. <https://doi.org/10.2514/6.2018-1082>
- Dabberdt WF, Ludwig FL, Johnson WBJ (1973) Validation and applications of an urban diffusion model for vehicular pollutants. *Atmos Environ* 7:603–618. [https://doi.org/10.1016/0004-6981\(73\)90019-X](https://doi.org/10.1016/0004-6981(73)90019-X)
- Fernandez F, Cleaver D, Gursul I (2021) Unsteady aerodynamics of a wing in a novel small-amplitude transverse gust generator. *Exp Fluids* 62(9). <https://doi.org/10.1007/s00348-020-03100-8>
- Figliola RS, Beasley DE (2012) Theory and design for mechanical measurements, 5th edn., chap 5. John Wiley and Sons, New York
- Fish F, Lauder G (2006) Passive and active flow control by swimming fishes and mammals. *Ann Rev Fluid Mech* 38:193–224. <https://doi.org/10.1146/annurev.fluid.38.050304.092201>
- Flay R, Stevenson D, Lindley D (1982) Wind structure in a rural atmospheric boundary layer near the ground. *J Wind Eng Ind Aerodyn* 10(1):63–78. [https://doi.org/10.1016/0167-6105\(82\)90054-X](https://doi.org/10.1016/0167-6105(82)90054-X)
- Garby L, Kuethe A, Shetzer J (1957) The generation of gusts in a wind tunnel and measurement of unsteady lift on an airfoil. Tech rep, US Air Force Wright Development Center
- Golubev VV, Visbal MR (2012) Modeling mav response in gusty urban environment. *Int J Micro Air Vehicles* 4(1):79–92. <https://doi.org/10.1260/1756-8293.4.1.79>
- Goman M, Khrabrov A (1994) State-space representation of aerodynamic characteristics of an aircraft at high angles of attack. *AIAA J* 31(5):1109–1115. <https://doi.org/10.2514/3.46618>

- Hamada Y, Saitoh K, Kobi N (2019) Gust alleviation control using prior gust information: wind tunnel test results. *Int Federat Auto Control Papers OnLine* 52(12):128–133. <https://doi.org/10.1016/j.ifacol.2019.11.125>
- Jing H, Liao H, Ma C et al (2020) Field measurement study of wind characteristics at different measuring positions in a mountainous valley. *Exp Thermal Fluid Sci*, 112. <https://doi.org/10.1016/j.expthermflusci.2019.109991>
- Kubo D (2018) Gust response evaluation of small uas via free-flight in gust wind tunnel. In: *AIAA SciTech Forum*, Kissimmee, FL, <https://doi.org/10.2514/6.2018-0297>
- Kussner HG (1935) Stresses produced in airplane wings by gusts. Tech rep, National Advisory Committee for Aeronautics
- Lancelot P, Sodja J, Werter N, et al (2015) Design and testing of a low subsonic wind tunnel gust generator. In: *International forum on aeroelasticity and structural dynamics*, St. Petersburg, Russia, <https://doi.org/10.12989/AAS.2017.4.2.125>
- Lentink D, Muller U, Stadhuis E et al (2007) How swifts control their glide performance with morphing wings. *Nature* 446:1082–1087. <https://doi.org/10.1038/nature05733>
- Mueller TJ, DeLaurier JD (2001) An overview of micro air vehicles aerodynamics. In: Zarchan P (ed) *Fixed and flapping wing aerodynamics for micro air vehicle applications*. Progress in Astronautics and Aeronautics, AIAA, New York, p 1–10, <https://doi.org/10.2514/5.9781600866654.0001.0010>
- Newman B (1958) Soaring and gliding flight of the black vulture. *J Exp Biol* 35(2):280–285. <https://doi.org/10.1242/jeb.35.2.280>
- Olson DA, Naguib AM, Koochesfahani MM (2020) Development of a low-turbulence transverse-gust generator in a wind tunnel. *AIAA J* 59(5):1575–1584. <https://doi.org/10.2514/1.J059962>
- Perotta G, Jones AR (2017) Unsteady forcing on a flat-plate wing in large transverse gusts. *Exp Fluids* 58:101. <https://doi.org/10.1007/s00348-017-2385-z>
- Quinn D, Kress D, Chang E, et al (2019) How lovebirds maneuver through lateral gusts with minimal visual information. In: *Proceedings of the National Academy of Sciences* 116(30):15,033–15,041. <https://doi.org/10.1073/pnas.1903422116>
- Rutensburg JW, Skinn DA, Tipps DO (2002) Statistical loads data for the airbus a-320 aircraft in commercial operations. Tech Rep FAA/AR-02/35, Department of Transportation/Federal Aviation Administration
- Sedky G, Jones AR, Lagor FD (2020) Lift regulation during transverse gust encounters using a modified Goman–Khrabrov model. *AIAA J* 58(9):3788–3798. <https://doi.org/10.2514/1.J059127>
- Selig Donovan, Fraser, (1989) *Airfoils at Low Speeds*. H A Stokely, Virginia Beach, VA
- Skinn D, Miedlar P, Kelly L (1996) Flight loads data for a boeing 737-400 in commercial operation. Tech. Rep. FAA/AR-95/21, Department of Transportation/Federal Aviation Administration
- Smith ZF, Jones AR, Hrynyuk JT (2018) Micro air vehicle scale gust-wing interaction in a wind tunnel. In: *AIAA SciTech Forum*, Kissimmee, FL, <https://doi.org/10.2514/6.2018-0573>
- Stutz CM, Bohl DG, Hrynyuk JT (2022) Investigation of lift forces during long gust interactions at low reynolds numbers. In: *AIAA SciTech Forum*, San Diego, CA, <https://doi.org/10.2514/6.2022-0042>
- Tucker VA (1987) Gliding birds: the effect of variable wing span. *J Exp Biol* 133:33–58. <https://doi.org/10.1242/jeb.133.1.33>
- Watkins S, Milbank J, Loxton BJ et al (2006) Atmospheric winds and their implications for microair vehicles. *AIAA J* 44(11):2591–2600. <https://doi.org/10.2514/1.22670>
- Watkins S, Mohamed A, Ol M (2019) Flight-relevant gusts: Computation-derived guidelines for mav ground test unsteady aerodynamics. In: *AIAA SciTech Forum*, San Diego, CA, <https://doi.org/10.2514/1.C035920>
- White C, Lim E, Watkins S et al (2012) A feasibility study of micro air vehicles soaring tall buildings. *J Wind Eng Ind Aerodyn* 103:41–49. <https://doi.org/10.1016/j.jweia.2012.02.012>
- Wieneke B (2015) Piv uncertainty quantification from correlation statistics. *Measure Sci Technol*, 26. <https://doi.org/10.1088/0957-0233/26/7/074002>
- Williams DR, Reissner F, Greenblatt D et al (2017) Modeling lift hysteresis on pitching airfoils with a modified Goman–Khrabrov model. *AIAA J* 55(2):403–409. <https://doi.org/10.2514/1.J054937>
- Williamson GA, McGranahan BD, Broughton BA, et al (2012) Summary of low-speed airfoil data—vol. 5. Tech rep, University of Illinois at Urbana Champagne
- Young AM, Smith AS (2020) The interaction of a sears-type sinusoidal gust with a cambered aerofoil in the presence of non-uniform streamwise flow. Tech. Rep. STO-TR-AVT-282, NATO Science and Technology Organization

Publisher's Note Springer Nature remains neutral with regard to jurisdictional claims in published maps and institutional affiliations.